Nanoscale

PAPER

View Article Online
View Journal | View Issue

Cite this: *Nanoscale*, 2021, **13**, 17386

A dual enzyme-mimicking radical generator for enhanced photodynamic therapy *via* series–parallel catalysis†

Zhenbang Cao,‡[a,b] Liang Zhang,‡[c] Jianxin Liu,[d] Dong Wang,*[c] Kang Liang,[a,b,e] Yu Chen[f] and Zi Gu*[a,b]

Received 24th June 2021,
Accepted 12th September 2021

DOI: 10.1039/d1nr04104e

rsc.li/nanoscale

Tumor hypoxia hampers the therapeutic efficacy of photodynamic therapy (PDT) by hardly supplying sufficient oxygen to produce cytotoxic compounds. Herein a dual enzyme-mimicking radical generator has been developed for the *in situ* generation of oxygen and abundant radical oxygen species to enhance PDT efficacy under photoacoustic imaging guidance. A manganese-incorporating and photosensitizer-loaded metal organic framework exhibited both catalase-like and peroxidase-like catalytic activities specifically at the tumor microenvironment, leading to simultaneous series catalysis and parallel catalysis pathways. As a result, the MOF-based radical generator nanoparticles can not only supply oxygen for PDT to produce singlet oxygen, but also generate hydroxyl radicals, thus further enhancing the anti-cancer effect of PDT. *In vitro* and *in vivo* evaluation of the radical generator nanoparticles demonstrated the relieved tumor hypoxia microenvironment, remarkably increased level of reactive oxygen species, and significantly improved anti-cancer effect with desirable PA imaging capacity. This work presents a "series–parallel catalysis" strategy enabled by a MOF nanozyme to enhance PDT efficiency and provides new insights into a highly efficient and low-toxic anti-cancer approach.

1. Introduction

Photodynamic therapy (PDT), being approved for clinical use in oncology, is an important non-invasive cancer treatment modality with high accuracy and safety.[1] PDT involves the combination of light, photosensitizer and oxygen (O_2). Upon light irradiation, the photosensitizer is excited from the ground state to the first excited single state and then converted to the triplet state. The excited triplet state can react with O_2 *via* electron transfer to generate singlet oxygen ($^1O_2$) that is able to kill cancer cells.[2] However, PDT efficacy is largely restricted by hypoxia (a hallmark of solid tumor in which the tissues are deprived of adequate O_2).[3,4] To address the issue of insufficient oxygen supply, a few strategies have been developed, including O_2 delivery (using hemoglobin,[5,6] perfluorocarbon[7]) and O_2 generation (using catalase-like nanoparticles such as MnO_2,[8,9] CaO_2,[10] Pt[11,12] to catalyze H_2O_2 into O_2 to alleviate tumor hypoxia). The catalase-like nanoparticle-based O_2 generation approach has been intensively explored in recent years, given that the involved nanomaterials not only act as the source to supply O_2 but also provide a versatile platform for multi-channeled treatment.[13] However, these nanoparticles suffer from low photosensitizer loading capacity, which implies a high dosage of nanoparticles required to achieve desirable therapeutic efficacy.

Another critical challenge that limits the practical application of PDT is the relatively weak oxidation ability of $^1O_2$, a therapeutic reactive oxygen species (ROS) generated through PDT. ROS, at a high level, can break the redox homeostasis and induce irreversible cancer cell damage, while a low level of ROS can stimulate cancer cell growth or be easily neutralized by endogenous antioxidants.[14,15] Therefore, the production of sufficient, highly active ROS is vital in PDT induced anticancer therapy. However, the main type of ROS in PDT is limited to $^1O_2$ ($E_0(^1O_2/O_2^{\bullet-})$ = 0.65 V), which has a weaker oxidation ability than many other types of ROS such as hydroxyl radicals ($E_0(^{\bullet}OH, H^+/H_2O)$ = 2.33 V). Thus, the production of highly oxi-

---

[a] School of Chemical Engineering, University of New South Wales, Sydney, NSW 2052, Australia. E-mail: zi.gu1@unsw.edu.au
[b] Australian Centre for NanoMedicine (ACN), University of New South Wales, Sydney, NSW 2052, Australia
[c] Department of Ultrasound, The First Affiliated Hospital of Chongqing Medical University, Chongqing 400010, P.R.China. E-mail: wang57554@163.com
[d] Ultrasound Department, The Central Hospital of Wuhan, Tongji Medical College, Huazhong University of Science and Technology, Wuhan, Hubei 430014, P.R.China
[e] Graduate School of Biomedical Engineering, University of New South Wales, Sydney, NSW 2052, Australia
[f] School of Life Sciences, Shanghai University, Shanghai 200444, P.R.China

† Electronic supplementary information (ESI) available. See DOI: 10.1039/d1nr04104e

‡ These authors contributed equally to this work.

dative $^{\bullet}$OH is ideal to be incorporated into the rational design of the PDT nanoplatform to boost therapeutic efficiency.

Aside from therapeutic consideration, PDT is a local cancer treatment operation that requires bio-imaging guidance.[16,17] Photoacoustic (PA) imaging is a newly emerging noninvasive biomedical imaging modality based on the generation of ultrasonic wave of ultrasound imaging, thus being able to provide high contrast imaging of the fine structure of deep tumors and anatomical, functional and metabolic information for tumor localization to guide local treatment such as PDT.[18,19]

Recently, metal–organic framework (MOF) nanomaterials have attracted wide attention and stood out among various nanomaterials for biomedical applications, by virtue of their unique structural, photonic and bio-nano interface characteristics.[20] MOFs are hybrid crystals composed of metal ions or clusters connected by multidentate organic ligands to form metal–organic arrays possessing a structure with very high porosity and enormous surface area that enable high drug loading capacity. MOFs are highly tunable in terms of chemical composition, crystal structure, morphology and porosity, which renders them the capacity to incorporate various functional metal ions and therapeutic agents for drug delivery, bioimaging, and multifunctional biomedical applications.[21,22] In this work, we developed a MOF74-based dual-enzyme mimicking radical generator (ICG@PEG-MnMOF74) that demonstrated enhanced PDT treatment of tumors (Fig. 1). The radical generator ICG@PEG-MnMOF74 particle consists of three key components that are manganese ion-doped MOF74, photosensitizer indocyanine green (ICG), and stabilizer polyethylene glycol (PEG). The key aspects of ICG@PEG-MnMOF74 directly attributed to the enhanced PDT performance include: (1) well-dispersed and nanosized ICG@PEG-MnMOF74 particles acting as a catalyst and a photosensitizer to trigger oxygen generation and subsequent self-oxygen supplement PDT that generated a large amount of cytotoxic $^1O_2$ ("series catalysis route"); (2) ICG@PEG-MnMOF74 particles exhibited peroxidase-like catalytic activities that induced a Fenton-like reaction to generate abundant $^{\bullet}$OH to kill cancer cells. The simultaneous production of $^1O_2$ and $^{\bullet}$OH leads to a "parallel catalysis route"; (3) both series and parallel catalysis routes occur in response to the tumor microenvironment conditions, leading to high tumor selectivity and specificity; and (4) ICG@PEG-MnMOF74 exhibited PA imaging functionality that enabled the accurate diagnosis and precision localization of tumors, serving as an imaging tool to guide PDT. Overall, the radical generator-mediated PDT approach *via* series and parallel catalysis routes not only makes up for the deficiencies of additional PDT but also introduces new therapeutic and imaging features, opening up an avenue for local cancer treatment.

2. Experimental methods

2.1. Materials

All chemicals, including manganese acetate tetrahydrate (>99.9%), 2,5-dihydroxyterephthalic acid (>98%), *N*,*N*-dimethyl-

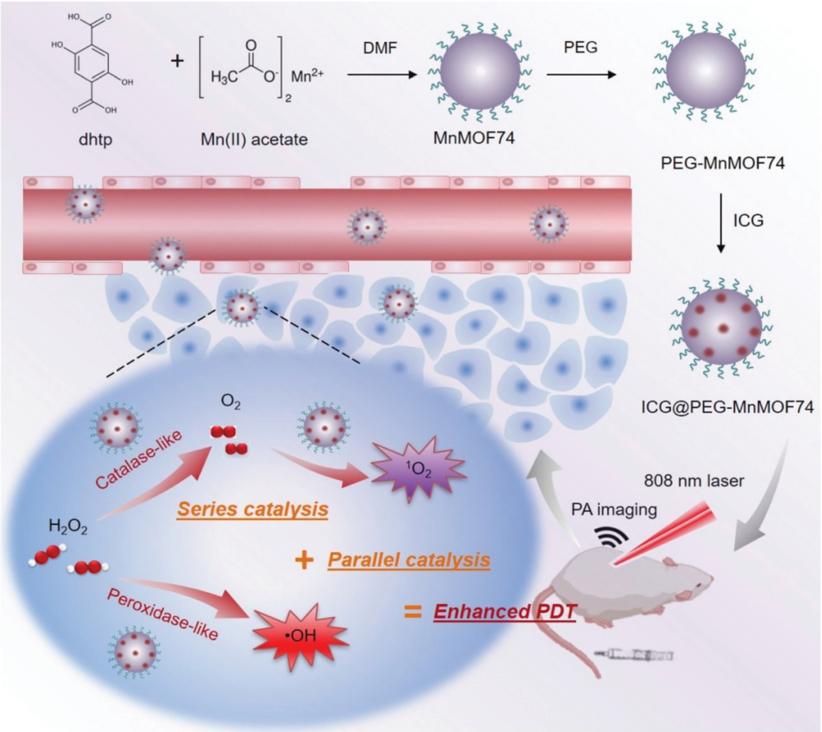

Fig. 1 Schematic illustration of the synthesis and enhanced photodynamic therapy (PDT) of ICG@PEG-MnMOF74 radical generator nanoparticles *via* series–parallel catalysis.

formamide, NaOH (≥98%), 3,3′,5,5′-tetramethylbenzidine (TMB), hydrogen peroxide (H_2O_2, 29.0–32.0%), hydrochloric acid (37%), acetic acid (≥99%), sodium acetate anhydrous (≥99%), phosphate buffered saline (PBS), paraformaldehyde, 2′,7′-dichlorofluorescein diacetate (DCFH-DA) and 2-(4-amidinophenyl)-6-indolecarbamidine dihydrochloride (DAPI, ≥98%) were purchased from Sigma-Aldrich. Dulbecco's modified Eagle's medium (DMEM), penicillin/streptomycin, and fetal calf serum (FCS) were purchased from Gibco. Phosphonic acid terminated poly(ethylene glycol) was synthesized using a controlled/living radical polymerization according to procedures described previously.[23,24] Milli-Q water was used in the experiments.

2.2. Synthesis of MnMOF74

Manganese acetate (1.3 mmol) and 2,5-dihydroxyterephthalic acid (dhtp) (0.5 mmol) were dissolved in 5 mL and 2.648 mL of *N*,*N*-dimethylformamide (DMF) respectively (the molar ratio of linker to metal = 2.6 : 1).[25] dhtp solution was added into manganese acetate solution in a dropwise manner under vigorous stirring at room temperature. After stirring for 20 h, the resultant was centrifuged with DMF, and then washed and centrifuged twice using methanol.

2.3. PEGylation of MnMOF74

To synthesize PEGylated MOF nanoparticles, the MnMOF74 slurry was dispersed in water and mixed with phosphate group-terminated poly (ethylene glycol) (PEG) at a PEG to MOF mass ratio of 2 : 1. The mixture was then sonicated in a water bath at room temperature for 30 min. The excessive PEG was removed *via* centrifugation. The resultant was dispersed in water and designated as PEG-MnMOF74.

2.4. ICG loading

Pre-dissolved ICG water solution was added into the PEG-MnMOF74 suspension at a mass ratio of 1 : 1. After mixing for 24 h *via* continuous stirring, the resultant was washed and collected by centrifugation, and denoted as ICG@PEG-MnMOF74. The loading capacity of ICG was calculated as the proportion of ICG in the total amount of ICG@PEG-MnMOF74.

2.5. Michaelis–Menten kinetics by TMB assay

TMB assay was conducted to monitor the chromogenic reaction (λ = 650 nm) of the MOF/H_2O_2 system. A solution (pH = 4) was prepared using HAC/NaAC in the presence of $NaHCO_3$ (25 mM). In an 800 μL buffer solution, 50 μg mL^{-1} of MOF suspension was mixed with TMB and H_2O_2 at the final concentrations of 800 μM and 1 mM respectively. The absorbance of the mixture was measured on a UV-vis spectrometer (CARY 300, Varian) equipped with a temperature controller. For the kinetic study, the concentrations of H_2O_2 (0.01, 0.05, 0.1, 0.2, 0.5, 1, 1.5, 2, 4, and 8 mM) were varied while the concentrations of TMB (800 μM) remained fixed. The Michaelis–Menten constant was calculated by using Lineweaver–Burk plots of the Michaelis–Menten equation:

$$\frac{1}{\nu} = \frac{K_m}{V_m} \times \left(C + \frac{1}{K_m}\right),$$

where ν represents the initial velocity, V_{max} the maximum reaction velocity, C the concentration of the substrate, and K_m the Michaelis–Menten constant.

2.6. Evaluation of H_2O_2 consumption

H_2O_2 consumption was evaluated by using the titanium sulfate ($Ti(SO_4)_2$) colorimetric method. PEG-MnMOF74 (0.25 mg) was incubated at 37 °C with 0.5 mL of H_2O_2 (1 mM), followed by mixing with a 25 mL solution containing 1.33 mL of $Ti(SO_4)_2$ (24%) and 8.33 mL of H_2SO_4 for 10 min. The mixture was then centrifuged to collect the supernatant, and the concentration of H_2O_2 in the supernatant was obtained by measuring the absorbance at λ = 405 nm. The continuous catalytic effect was measured by the repetitive addition of H_2O_2 (1 mM) to the solution.

2.7. Cell culture

Breast cancer cells (4T1 cells) were cultured in a growth medium (DMEM) supplemented with 10% fetal calf serum (FCS), streptomycin (100 mg mL^{-1}) and penicillin (100 units mL^{-1}). The cells were cultured at 37 °C in a humidified atmosphere with 5% CO_2 in air.

2.8. *In vitro* and *in vivo* photoacoustic imaging

The PA imaging of ICG@PEG-MnMOF74 was conducted on a Vevo LAZR Photoacoustic Imaging System (VisualSonics Inc., Toronto, Canada) equipped with a LZ250 (fiber-optic bundles: 25.4 × 1.25 mm; focal depth: 10 mm; center frequency: 21 MHz; axial resolution: 75 μm). Prior to imaging, 100 μg mL^{-1} ICG@PEG-MnMOF74 was scanned under PA at different wavelengths from 690 nm–960 nm to determine the λ_{max}. ICG of certain concentrations was subjected to PA imaging with regard to the region of interest (ROI). For the *in vivo* PA imaging, 4T1 tumor-bearing Balb/c mice (n = 3) were intravenously injected with 200 μL of saline containing ICG@PEG/MOF (4 mg kg^{-1} ICG, 10 mg kg^{-1} PEG-MnMOF74). After injection, PA images of tumor sites were recorded at λ_{max} = 780 nm at 1, 2, 4, 6, 8 and 24 h. The intensities in the ROI were quantified using Vevo LAZR software.

2.9. *In vitro* cell viability assessment

The *in vitro* cytotoxicity was assessed by CCK-8 assay. The 4T1 cells were treated with ICG and ICG@PEG-MnMOF74 at a concentration equivalent to 5, 10 or 15 μg mL^{-1} of ICG containing 25 mM $NaHCO_3$. After 6 h of incubation, the cells were irradiated at a power of 1.5 W cm^{-2} for 3 min on ice (excluding the photothermal effect). The cell viability was measured by using a CCK-8 cell viability kit and calculated by comparing with the control group without treatment. The cell living status was also visualized by live and dead staining with calcein acetoxymethyl ester (CAM) and propidium iodide (PI) to differentiate live (green fluorescence) and dead (red fluorescence) cells. Images were recorded with a confocal laser scanning microscope (FV 1000, Olympus, Japan). Cell quantification was conducted using ImageJ. Live and dead cells in 3 randomly selected views with equivalent areas were counted. The percentages were calculated as live cell percentage = live cells/(live cells + dead cells) × 100%.

2.10. *In vitro* oxidative stress assessment

The hydroxyl radical generation ability of PEG-MnMOF74 under the tumor microenvironment conditions was evaluated by using a hydroxyphenyl fluorescein (HPF) probe. The 4T1 cells were seeded at a density of 1×10^5 in DMEM in the φ 15 CLSM-exclusive culture disk and allowed to adhere overnight. The cells were treated with different agents (*i.e.,* PBS, H_2O_2 (100 μM), PEG-MnMOF74 (25 μg mL^{-1}), PEG-MnMOF74 (25 μg mL^{-1}) + H_2O_2 (100 μM)). After incubation for 6 h, the cells were cultured with HPF solutions (10 μL of 1 mM per mL culture) for 30 min. The level of the intracellular hydroxyl radical was evaluated with confocal microscopy by detecting the fluorescence at λ_{ex} = 488 nm and λ_{em} = 525 nm. The experiments were carried out in 25 mM $NaHCO_3$ cultures with various pH values.

The *in vitro* oxidative stress level was assessed using 2′,7′-dichlorofluorescein diacetate (DCFH-DA). The 4T1 cells were seeded at a density of 1×10^5 in DMEM in the φ 15 CLSM-exclusive culture disk and allowed to adhere overnight. The culture medium was then replaced with media containing ICG@PEG-MnMOF74 or ICG at a concentration equivalent to 10 μg mL^{-1} of ICG. Five treatments (*i.e.,* PBS, H_2O_2 (100 μM), H_2O_2 (100 μM) + laser irradiation, ICG + H_2O_2 (100 μM) + laser irradiation, PEG-MnMOF74 + H_2O_2 (100 μM), and ICG@PEG-MnMOF74 + H_2O_2 (100 μM) + laser irradiation) were performed to evaluate the *in vitro* oxidative stress. After incubation for 6 h, the cells were incubated with DCFH-DA (30 μM) for 30 min. Laser irradiation was then conducted on selected groups at a power of 1.5 W cm^{-2} for 3 min on ice. The level of intracellular ROS was evaluated with confocal microscopy by detecting the fluorescence of DCF (λ_{ex} = 488 nm, λ_{em} = 525 nm for DCFH-DA).

2.11. *In vivo* biosafety study

All animal procedures were performed in accordance with the Guidelines for Care and Use of Laboratory Animals of Chongqing Medical University and experiments were performed with the approval of the Animal Ethics Committee of The First Affiliated Hospital of Chongqing Medical University. 7-Week female Balb/c mice (~20 g) were intravenously injected with 200 μL of ICG@PEG-MnMOF74 saline solution at the dosages of 10, 40 and 80 mg kg^{-1} with the same volume of saline as the control. At 30-day post-treatment, blood was collected for hematological and biomedical index analysis. Mice were then sacrificed to collect their major organs (heart, liver, spleen, lungs, and kidneys) in 4% paraformaldehyde solution for histopathology analysis (hematoxylin and eosin (H&E) staining assay).

2.12. *In vivo* anti-cancer effect evaluation

Xenografted tumors were generated in female Balb/c mice (~20 g, 7 weeks old) by subcutaneously inoculating 1×10^6 4T1 cells suspended in PBS (100 μL). Once the tumor reached a volume of 100 mm^3, mice per group were randomly allocated to 5 groups (n = 5): saline (group I), laser (group II), ICG + laser (group III), ICG@PEG-MnMOF74 (group IV), ICG@PEG-MnMOF74 + laser (group V). ICG and ICG@PEG-MnMOF74 in saline were injected *via* the tail vein (200 μL, 4 mg kg^{-1} ICG). After 6 h, the mice from group II, III and V were irradiated at the site of tumors with an 808 nm laser (1.5 W cm^{-2}, on 20 s, off to room temperature, a total of 10 min on). Tumors were measured every two days with a digital caliper. The tumor volumes (V) were calculated as $V = L \times W^2/2$, and also normalized to the initial volume (V_0) to obtain the relative tumor volume (V/V_0). Mice were euthanized once the tumor volume reached 1000 mm^3.

2.13. *In vivo* detection of tumor hypoxia status

To visualize the hypoxia status of the 4T1 tumor, 6 mice were randomly divided into 2 groups (control and ICG@PEG-MnMOF74, n = 3 in each group). The two groups were intravenously injected with saline and ICG@PEG-MnMOF74 (4 mg kg^{-1} ICG, 10 mg kg^{-1} PEG-MnMOF74) respectively. The oxygenated hemoglobin levels of tumor tissues at 1, 2, 4, 6, 8, and 24 h post-injections were evaluated using a Vevo LAZR PA imaging system in oxy-hem mode and oxyhemoglobin saturation (sO_2 Avr Total). It was recorded by measuring the ratios of oxygenated hemoglobin (λ = 850 nm) and deoxygenated hemoglobin (λ = 750 nm). At 6 h post-injection, the tumor tissues were collected for HIF-1α staining with the red fluorescence indicating hypoxia regions.

2.14. Characterization

The size distribution and zeta potential were measured using a Malvern Zetasizer Nano Series. X-ray diffraction (XRD) measurements were performed on PEG/MOF powders using a PANalytical Empyrean II Co Source XRD instrument operated at 45 kV and 40 mA and a scan rate of 0.01° min^{-1} applied with a step size of 2θ = 0.0260°. The morphology of nanoparticles was observed using a transmission electron microscope (TEM, FEI Tecnai G2) at an acceleration voltage of 200 kV. Thermogravimetric analysis (TGA, TA Instruments, Q5000) was performed under nitrogen 40 mL min^{-1} from 30 to 800 °C with a rate of 20 °C min^{-1}. The manganese content was measured on a PerkinElmer OPTIMA 7300 inductively coupled plasma optical emission spectrometer (ICP-OES) after the dissolution of the MOF in 1 M hydrochloride acid. The concentration of ICG was measured at a wavelength of 780 nm on a SpectraMax paradigm multimode microplate reader. O_2 generation was monitored by using a dissolved oxygen meter (HANNA HI 98193). Electron spin resonance (ESR) spectra were obtained at room temperature in perpendicular mode on a Bruker EMX-8/2.7 spectrometer with the following settings: microwave frequency = 9.773 GHz, microwave power = 6.325 mW, modulation frequency = 100.00 kHz and modulation amplitude = 2.00 G. DMPO was used as a spin trap. The experiment was carried out in 25 mM $NaHCO_3$/5% CO_2 solution systems with various pH values.

2.15. Statistical analysis

Quantitative data are presented as mean ± SEM and analyzed by two-way ANOVA with Tukey's multiple comparisons test using GraphPad Prism software; a P-value <0.05 was considered statistically significant ($^*P < 0.05$, $^{**}P < 0.01$, and $^{***}P < 0.001$).

3. Results and discussion

3.1. Synthesis and physicochemical structure of ICG@PEG-MnMOF74

The radical generator for enhanced PDT was designed and synthesized by incorporating Mn ions and photosensitizer ICG into a MOF74 structure. Mn-containing MOF74 was firstly synthesized by the copolymerization of manganese ions with dimethylformamide links, and stabilized by the surface modification of PEG and loaded with photosensitizer ICG. MnMOF74 particles exhibited a suborbicular morphology with the particle size being about 50 nm (Fig. 2a and b), and PEG-MnMOF74 appeared less aggregated than MnMOF74 (ESI Fig. S1†). Such improved dispersity after PEG coating is also demonstrated by the relatively narrow hydrodynamic size distribution of PEG-MnMOF74 (176 nm in average size and 0.08 in PDI (Fig. 2c), compared with MnMOF74 being 342 nm in size and 0.27 in PDI). PEG modification not only increased MnMOF74 particle dispersity in water but also alleviated severe aggregation in electrolyte solutions (*i.e.* saline, PBS, culture medium containing serum) (ESI Table S1†). The XRD patterns of both PEG-MnMOF74 and MnMOF74 particles

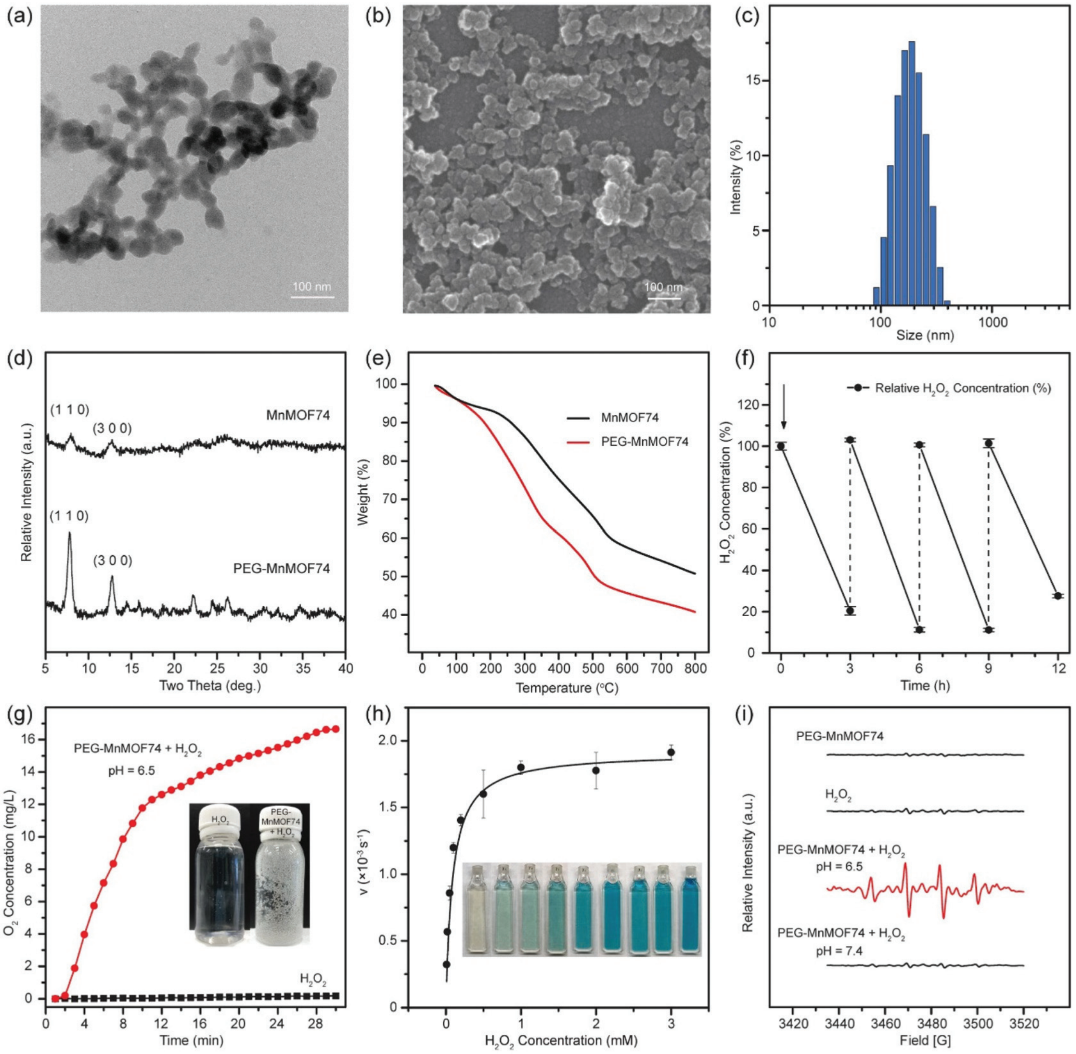

Fig. 2 Physicochemical structure and catalytic characterization of radical generator nanoparticles. (a) TEM image, (b) SEM image, and (c) DLS of PEG-MnMOF74. (d) XRD pattern and (e) TGA profiles of MnMOF74 and PEG-MnMOF74. (f) Repetitive catalytic ability of PEG-MnMOF74 with the repetitive addition of H_2O_2. (g) O_2 generation from mixing PEG-MnMOF74 and H_2O_2, compared to H_2O_2 alone. The insert photograph shows H_2O_2 solutions with (right) and without (left) PEG-MnMOF74. (h) Michaelis–Menten steady-state kinetics by plotting reaction velocity (v) against H_2O_2 concentration. The insert is a compilation of digital photos of the aliquots captured at the end of each reaction. (i) ESR spectra of PEG-MnMOF74 solution, H_2O_2 solution, and PEG-MnMOF74 with the addition of H_2O_2 in the buffers of pH 6.5 and pH 7.4.

showed characteristic peaks at 2θ = 7.8° and 2θ = 12.7° that are associated with reflection from the (110) and (300) planes (Fig. 2d).[26] The sharp peaks in the XRD pattern of PEG-MnMOF74 indicated that PEG-MnMOF74 particles were well crystallized. The XPS spectrum revealed the co-existence of Mn, O and C elements in both PEG-MnMOF74 and MnMOF74 (ESI Fig. S2†). ICP and TGA analysis showed that the Mn ions and PEG molecules account for 19.29 wt% and 11 wt% respectively in PEG-MnMOF74 (Fig. 2e). The successful loading of ICG in PEG-MnMOF74 was monitored by UV-vis spectroscopy, and the loading capacity of ICG was calculated to be approximately 28.6 wt%.

3.2. Dual enzyme-like property of PEG-MnMOF74

Manganese is a versatile transition metal with bioactive catalytic activities. In nature, Mn functions in the oxygen-evolving complex of photosynthesis.[27] Mn serves as a cofactor in many enzymes, and a trace metal required for the normal growth and development of human beings.[27] The ability of Mn-containing nanomaterials to catalyze H_2O_2 to O_2 has been recently explored for biomedical applications.[28,29] Given that PEG-MnMOF74 particles have a high content of Mn (~20 wt%), PEG-MnMOF74 can serve as a desirable catalase-mimicking nanozyme agent. The catalase-like activity of PEG-MnMOF74 was evaluated by measuring H_2O_2 consumption and recording the dissolved O_2 level (Fig. 2f and g). The results from the H_2O_2 consumption study showed that ~80% of H_2O_2 was consumed within 3 h after the first addition of H_2O_2, indicating the high degree of catalytic efficiency of PEG-MnMOF74 (Fig. 2f). After three cycles of H_2O_2 addition and consumption, PEG-MnMOF74 still remained efficient catalytic activity that was able to decompose ~73% of H_2O_2. The ability of PEG-MnMOF74 to generate O_2 from H_2O_2 was assessed by recording the amount of O_2 production using an oxygen probe (Fig. 2g). The addition of PEG-MnMOF74 in H_2O_2 solution induced the rapid generation of O_2 and reached 17 mg L^{-1} after 30 min reaction, while the dissolved O_2 in water in the absence of PEG-MnMOF74 remained at a basal level.

Based on the fact that Mn(II) is a Fenton-like catalyst,[30,31] we investigated the peroxidase-like activity of PEG-MnMOF74 to disproportionate H_2O_2 to $^{\bullet}$OH. A typical chromogenic reaction of TMB was used to evaluate the peroxidase-like activity of PEG-MnMOF74 particles qualitatively and quantitatively

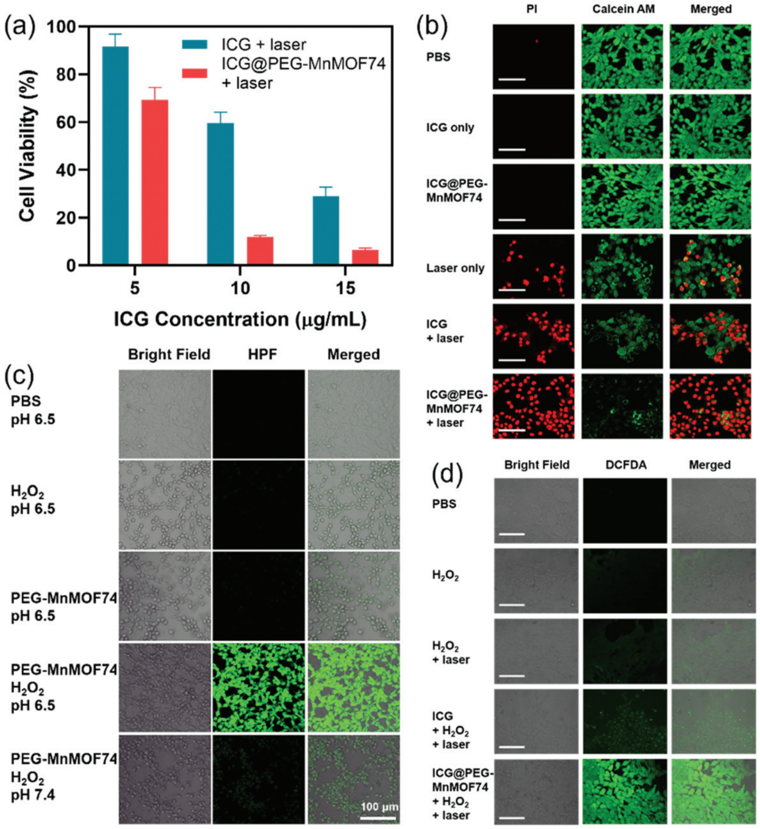

Fig. 3 *In vitro* evaluation of PDT mediated by ICG@PEG-MnMOF74. (a) Cell viability of ICG and ICG@PEG-MnMOF74 with 808 nm laser irradiation. (b) Confocal images of 4T1 cells treated with PBS, ICG (10 μg mL^{-1}) and ICG@PEG-MnMOF74 (containing 10 μg mL^{-1} ICG) with or without 808 nm laser irradiation. Green and red fluorescence indicate live and dead cells *via* CAM and PI staining. (c) Confocal images of 4T1 cells stained with a hydroxyl radical indicator hydroxyphenyl fluorescein (HPF) under different treatment conditions. Green fluorescence indicates the level of intracellular hydroxyl radical generation. (d) Confocal images of 4T1 cells stained with a ROS indicator DCFH-DA under different treatment conditions. Green fluorescence indicates the level of intracellular ROS generation. Scale bar = 100 μm.

(Fig. 2h). The TMB solution turned blue with the addition of PEG-MnMOF74 and H_2O_2, and the blue color became darker with the increase of either reaction time or H_2O_2 concentration. This phenomenon was caused by $^{\bullet}OH$ generation during H_2O_2 decomposition that oxidizes TMB to a blue product (with light absorption λ_{max} 650 nm). The absorbance at λ = 650 nm was plotted against time with the addition of H_2O_2 at different concentrations into PEG-MnMOF74, and the initial velocities were calculated. The initial velocities against H_2O_2 concentration were fitted into the Michaelis–Menten equation, and the Michaelis–Menten constant (K_m) and maximum velocity (V_{max}) were calculated as 0.055 mM and 1.86×10^{-6} M s^{-1} respectively, indicating the high catalytic activity of converting H_2O_2 to $^{\bullet}OH$. The K_m value of 0.055 mM indicates that the PEG/Fe-LDH nanocatalyst could achieve 50% of maximum catalytic activity at the H_2O_2 concentration as low as 0.055 mM, which is lower than the typical H_2O_2 concentration in the tumor microenvironment (0.1 mM). The Vmax of PEG-MnMOF74 indicates that the PEG-MnMOF74 could catalyze H_2O_2 at the maximum velocity of 1.86×10^{-6} M s^{-1}. Next, the radical species from the catalytic reaction was identified by electron spin resonance (ESR) spectroscopy with 5,5-dimethyl-1-pyrroline *N*-oxide (DMPO) as a spin trap (Fig. 2i). The ESR spectrum of PEG-MnMOF74 solution with the addition of H_2O_2 under pH 6.5 showed a characteristic 1 : 2 : 2 : 1 hydroxyl radical signal, while this signal was not observed in the ESR spectra under pH 7.4. This acidity-triggered $^{\bullet}OH$ generation indicates the potential use of PEG-MnMOF74 as a tumor-selective ROS generator to specifically kill cancer cells. The intracellular catalytic generation of $^{\bullet}OH$ *via* PEG-MnMOF74 was verified by using a highly reactive oxygen radical probe hydroxyphenyl fluorescein (HPF). The cells displayed strong green fluorescence with PEG-MnMOF74 in the presence of H_2O_2 at pH 6.5 (Fig. 3c). In contrast, a low level of fluorescence signal was observed in the cells with the control treatments (Fig. 3c). The results indicate the stimuli-responsive intracellular hydroxyl radical generation ability of PEG-MnMOF74 in the tumor microenvironment.

3.3. *In vitro* assessment of enhanced PDT

The PDT assessment of ICG@PEG-MnMOF74 was performed on breast cancer 4T1 cells, and the cell viability was assessed by both CCK-8 assay and CAM/PI (live/dead) cell staining. From CCK-8 results (Fig. 3a), ICG@PEG-MnMOF74 demonstrated significantly stronger inhibition on 4T1 cell growth than pure ICG treatment at ICG concentrations of 5, 10 and 15 μg mL^{-1} under laser irradiation. For example, at an ICG concentration of 10 μg mL^{-1}, cell viability was 11.9% in the ICG@PEG-MnMOF74 + laser group, which was remarkably lower than 59.8% in the ICG + laser group. In comparison, PEG-MnMOF74 demonstrated cell growth inhibition only at the concentrations being higher than 25 μg mL^{-1} (ESI Fig. S3†), indicating that the combination of ICG and PEG-MnMOF74 enhances the anticancer effect. By staining cells with living/dead cell dyes, negligible dead cells were found in the treatment groups of laser only and ICG@PEG-MnMOF74, as indicated by the strong green fluorescence of calcein-AM staining and few red fluorescence of PI staining (Fig. 3b). The treatment of ICG + laser led to an increased number of dead cells, suggesting that the combination of ICG and laser irradiation has shown a certain photodynamic effect. Notably, the ICG@PEG-MnMOF74 + laser exhibited a remarkably enhanced photodynamic effect that led to significantly increased cell death, in comparison to other treatments. In addition, results from the live cell quantifi-

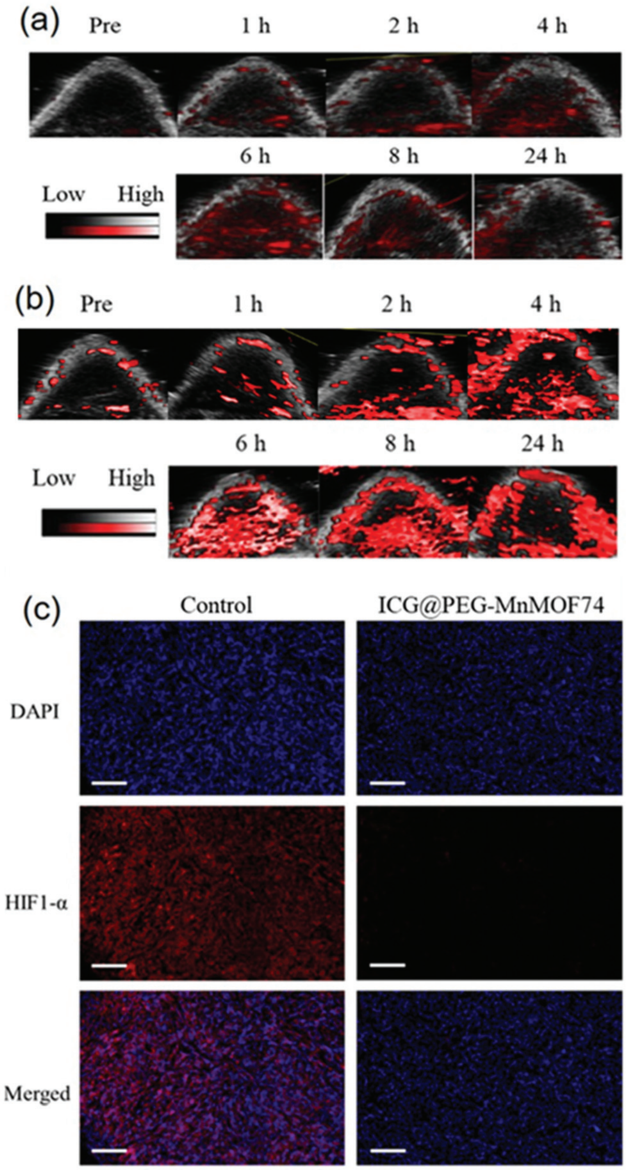

Fig. 4 *In vivo* PA imaging of ICG@PEG-MnMOF74 nanoparticles in 4T1 tumor bearing mice. (a) *In vivo* PA images of tumor tissues at different time intervals after the intravenous injection of ICG@PEG-MnMOF74. (b) *In vivo* tumor oxygenation before and after the intravenous injection of ICG@PEG-MnMOF74 was detected by PA imaging in the oxyhemoglobin mode. (c) Immunofluorescence images of tumor tissues stained by a hypoxia probe HIF1-α and DAPI. Scale bar = 100 μm.

cation of the fluorescence images (ESI Fig. S4†) correspond to the cell viability results from the CCK-8 assay.

To further explore the active compound that induces cell death, intracellular ROS generation was characterized by the DCFH-DA probe that could be rapidly oxidized by $^1O_2$ and $^\bullet OH$ and emit green fluorescence acting as a $^1O_2$ and $^\bullet OH$ sensor (Fig. 3d). The confocal images showed that only the ICG@PEG-MnMOF74 + laser group exhibited strong green fluorescence that was obviously much weaker in other control groups, indicating the significant production of ROS in 4T1 cells treated by ICG@PEG-MnMOF74 and laser. This phenomenon is in accordance with the aforementioned cell viability results, and highlights the indispensable role of MnMOF74 in the enhanced PDT approach.

3.4. *In vivo* assessment of enhanced PDT

In vivo anticancer behavior and photoacoustic imaging performance of ICG@PEG-MnMOF74 were evaluated using a 4T1 xenograft mouse model. Firstly, using ICG@PEG-MnMOF74 as a diagnostic agent has been explored by evaluating PA signals. The PA signal intensity increased in a linear relationship with the concentration of ICG@PEG-MnMOF74 (ESI Fig. S5†), demonstrating desirable PA responses. The *in vivo* PA images of tumor tissues showed that the PA signal increased gradually after the intravenous administration of ICG@PEG-MnMOF74, and the PA signal intensity reached the maximal at 6 h post-injection (Fig. 4a). The bio-imaging results imply the promising application of ICG@PEG-MnMOF74 to guide PDT treatment. Prior to performing PDT *in vivo*, we confirmed the ability of ICG@PEG-MnMOF74 to alleviate tumor hypoxia *in vivo*. The first line of evidence came from PA imaging in the oxyhemoglobin mode that was used to detect the oxygenated hemoglobin level of tumors before and after the administration of ICG@PEG-MnMOF74 (Fig. 4b). Before injecting ICG@PEG-MnMOF74, oxyhemoglobin showed weak signal intensity. The signal increased significantly after the administration of ICG@PEG-MnMOF74 and lasted for over 24 h. The PA imaging of tumor tissues in the oxyhemoglobin mode clearly showed that ICG@PEG-MnMOF74 could effectively improve oxygenation in hypoxic tumor regions. The hypoxia-inducible factor (HIF)-1α staining was conducted to form our second line of evidence to support the effect of ICG@PEG-MnMOF74 to alleviate tumor hypoxia. The tumors of mice treated with ICG@PEG-MnMOF74 exhibited very weak

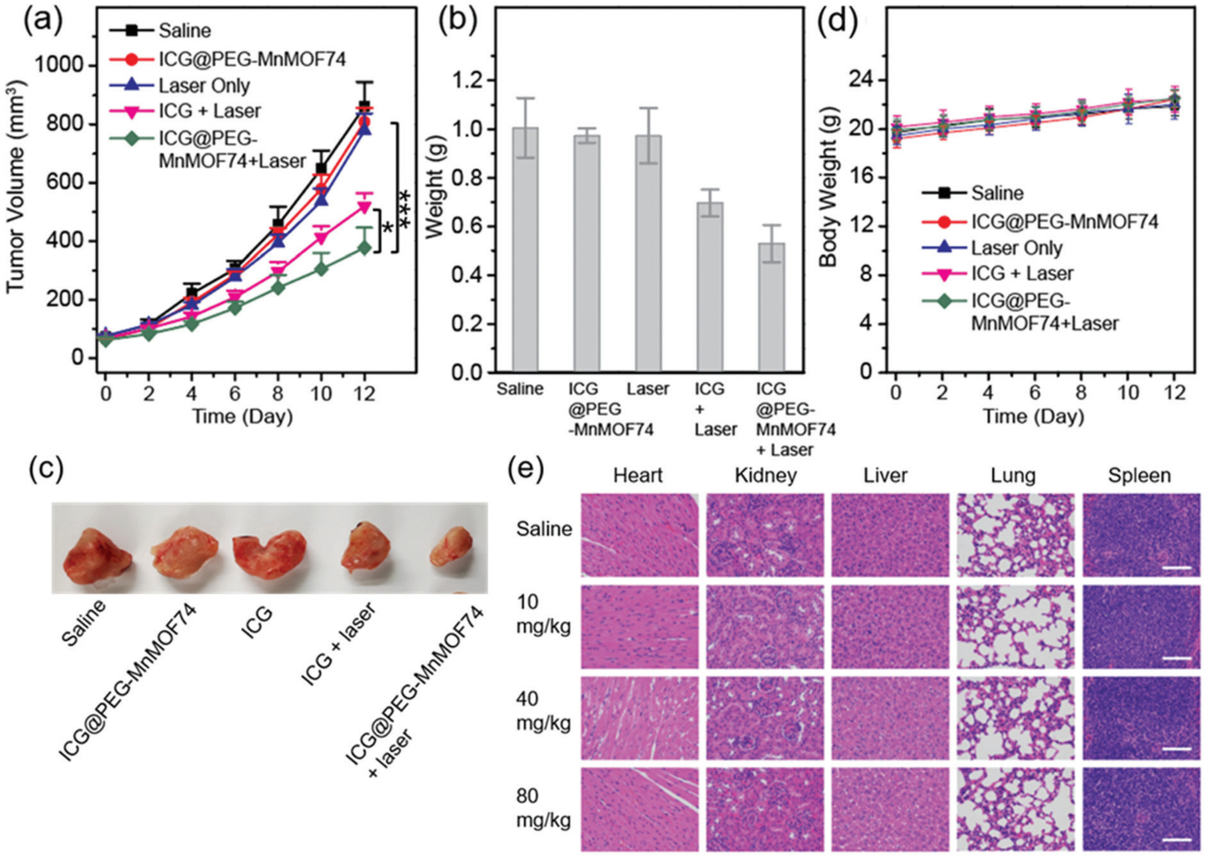

Fig. 5 *In vivo* therapeutic effect and biosafety evaluation of ICG@PEG-MnMOF74. (a) Tumor volume and (b) tumor weight of 4T1 tumor-bearing Balb/c mice with the intravenous injection of saline, ICG and ICG@PEG-MnMOF74 with or without 808 nm laser irradiation. $^*P < 0.05$, $^{**}P < 0.01$, and $^{***}P < 0.001$. (c) Representative images of tumor tissues collected after different treatments for 12 days. (d) Body weight of Balb/c under different treatment conditions. (e) Histological images of major organ tissues (heart, kidneys, liver, lungs, and spleen) collected at 30-day post-injection of ICG@PEG-MnMOF74 at different doses. Scale bar = 100 μm.

red fluorescence of HIF-1α and thus showed a low level of hypoxia, while the tumor tissues treated with the saline control exhibited a strong HIF-1α signal and a high level of hypoxia (Fig. 4c). All above results demonstrated that ICG@PEG-MnMOF74 could trigger *in vivo* localized oxygen generation efficiently and increase the level of endogenous oxygen level that can be beneficial to enhance PDT performance.

In vivo PDT evaluation was conducted by treating 4T1-tumor bearing mice with different treatments including saline, laser only, ICG@PEG-MnMOF74 (14 mg kg^{-1} containing ICG 4 mg kg^{-1}), ICG (4 mg kg^{-1}) + laser, and ICG@PEG-MnMOF74 (14 mg kg^{-1}) + laser. ICG@PEG-MnMOF74 exhibited the obvious inhibition of tumor growth after intravenous injection under laser irradiation, demonstrated by the significantly smaller tumor size than other groups (Fig. 5a–c). In particular, at the end of the treatment period, the average tumor volume of the ICG@PEG-MnMOF74 + laser group was about 2.7-fold smaller than that of the saline group (Fig. 5a). The enhanced anti-cancer effect induced by the ICG@PEG-MnMOF74 could be largely attributed to dual enzyme-like activities of PEG-MnMOF74 by simultaneously producing O_2 and ROS ($^1O_2$ and $^{\bullet}OH$).

To evaluate *in vivo* biosafety, Balb/c mice were intravenously injected with ICG@PEG-MnMOF74 at a low dose of 10 mg kg^{-1}, a medium dose of 40 mg kg^{-1}, and a high dose of 80 mg kg^{-1}. At 30-day post-injection, the major organs (heart, liver, spleen, lungs and kidneys) were collected for histological analysis. H&E staining images of tissues with the ICG@PEG-MnMOF74 treatment showed no observable pathological abnormalities (Fig. 5e), signifying the biocompatibility of ICG@PEG-MnMOF74. Also, the blood of mice was collected after a 30-day treatment period for complete blood count and biochemical index analysis including liver functional markers (ALT, AST, and TBIL), kidney functional markers (BUN and CR), and myocardial enzyme spectrum (CK and LDH-L). The results showed negligible variation among the different groups, indicating undetectable toxicity in a relatively long timeframe (ESI Fig. S6†). Moreover, the body weight of all mice increased regularly and demonstrated no significant change amongst groups (Fig. 5d). All these results indicated that the ICG@PEG-MnMOF74 has desirable *in vivo* biocompatibility.

4. Conclusions

This work presented a “series–parallel catalysis” strategy that simultaneously produced O_2 and $^{\bullet}OH$ to alleviate tumor hypoxia and generate abundant radicals for the enhanced PDT of cancers. It is realized by developing a dual-enzyme mimicking radical generator ICG@PEG-MnMOF74 that was constructed *via* a facile method and demonstrated both catalase-like and peroxidase-like activities. Both *in vitro* and *in vivo* experiments, using breast cancer 4T1 cell and animal models, exhibited the ability of ICG@PEG-MnMOF74 to overcome hypoxia and generate abundant ROS to specifically and efficiently kill cancer cells. The PA imaging functionality of ICG@PEG-MnMOF74 further guaranteed the precision localization of the tumor for improved PDT performance. We envisage that this multi-channeled radical generation strategy, along with the multifunctional dual-enzyme-like nanoplatform, will open the door to promote precise and effective PDT outcome.

Author contributions

Z. Gu initiated and conceived the project. Z. Gu and D. Wang oversaw and were in charge of research activities at their own institutes. Z. Cao and L. Zhang performed the experiments and data analysis: Z. Cao was in charge of nanoparticle synthesis, characterisation and *in vitro* studies, and L. Zhang conducted animal experiments and part of cell studies. K. Liang, J. Liu and Y. Chen provided technical support on experimental design. All the authors contributed to manuscript writing.

Conflicts of interest

There are no conflicts to declare.

Acknowledgements

This work was financially supported by the National Health and Medical Research Council of Australia (NHMRC) Early Career Fellowship (APP1073591), University of New South Wales (UNSW) Engineering Faculty Research Fund, UNSW-CAS (Chinese Academy of Sciences) Collaborative Research Grant, Chongqing Natural Science Foundation (cstc2019jcyj-zdxmX0019), and Health Commission of Hubei Province Scientific Research Project (Grant No. WJ2019M030). The authors acknowledge the UNSW Mark Wainwright Analytical Centre including facilities supported by the Australian Microscopy & Microanalysis Research Facility (AMMRF) at the Electron Microscope Unit.

References

1 A. P. Castano, P. Mroz and M. R. Hamblin, *Nat. Rev. Cancer*, 2006, **6**, 535.
2 X. Qian, Z. Gu and Y. Chen, *Mater. Horiz.*, 2017, **4**, 800.
3 T. Wang, H. Zhang, Y. Han, H. Liu, F. Ren, J. Zeng, Q. Sun, Z. Li and M. Gao, *ACS Appl. Mater. Interfaces*, 2019, **11**, 16367.
4 C. E. Weber and P. C. Kuo, *Surg. Oncol.*, 2012, **21**, 172.
5 Z. Luo, M. Zheng, P. Zhao, Z. Chen, F. Siu, P. Gong, G. Gao, Z. Sheng, C. Zheng and Y. Ma, *Sci. Rep.*, 2016, **6**, 1.
6 S. Wang, F. Yuan, K. Chen, G. Chen, K. Tu, H. Wang and L. Wang, *Biomacromolecules*, 2015, **16**, 2693.
7 Y. Cheng, H. Cheng, C. Jiang, X. Qiu, K. Wang, W. Huan, A. Yuan, J. Wu and Y. Hu, *Nat. Commun.*, 2015, **6**, 1.
8 W. Zhu, Z. Dong, T. Fu, J. Liu, Q. Chen, Y. Li, R. Zhu, L. Xu and Z. Liu, *Adv. Funct. Mater.*, 2016, **26**, 5490.

9 P. Prasad, C. R. Gordijo, A. Z. Abbasi, A. Maeda, A. Ip, A. M. Rauth, R. S. DaCosta and X. Y. Wu, *ACS Nano*, 2014, **8**, 3202.

10 L. H. Liu, Y. H. Zhang, W. X. Qiu, L. Zhang, F. Gao, B. Li, L. Xu, J. X. Fan, Z. H. Li and X. Z. Zhang, *Small*, 2017, **13**, 1701621.

11 J. Wei, J. Li, D. Sun, Q. Li, J. Ma, X. Chen, X. Zhu and N. Zheng, *Adv. Funct. Mater.*, 2018, **28**, 1706310.

12 S. Xu, X. Zhu, C. Zhang, W. Huang, Y. Zhou and D. Yan, *Nat. Commun.*, 2018, **9**, 1.

13 X. Li, N. Kwon, T. Guo, Z. Liu and J. Yoon, *Angew. Chem., Int. Ed.*, 2018, **57**, 11522.

14 H.-U. Simon, A. Haj-Yehia and F. Levi-Schaffer, *Apoptosis*, 2000, **5**, 415.

15 K. Apel and H. Hirt, *Annu. Rev. Plant Biol.*, 2004, **55**, 373.

16 M. Ethirajan, Y. Chen, P. Joshi and R. K. Pandey, *Chem. Soc. Rev.*, 2011, **40**, 340.

17 B. Yang, Y. Chen and J. Shi, Nanocatalytic Medicine, *Adv. Mater.*, 2019, **31**, 1901778.

18 I. Steinberg, D. M. Huland, O. Vermesh, H. E. Frostig, W. S. Tummers and S. S. Gambhir, *Photoacoustics*, 2019, **14**, 77.

19 Q. R. Fu, R. Zhu, J. B. Song and H. H. Yang, *Adv. Mater.*, 2019, **31**, 1805875.

20 J. Yang and Y. W. Yang, *Small*, 2020, **16**, 1906846.

21 W. Cai, H. Gao, C. Chu, X. Wang, J. Wang, P. Zhang, G. Lin, W. Li, G. Liu and X. Chen, *ACS Appl. Mater. Interfaces*, 2017, **9**, 2040.

22 Z. Guo, T. Wang, A. Rawal, J. Hou, Z. Cao, H. Zhang, J. Xu, Z. Gu, V. Chen and K. Liang, *Mater. Today*, 2019, **28**, 10.

23 Z. Cao, L. Liang, K. Liang, S. Cheong, C. Boyer, J. J. Gooding, Y. Chen and Z. Gu, *Adv. Sci.*, 2018, **5**, 1801155.

24 Z. Cao, N. N. K. Adnan, G. Wang, A. Rawal, B. Shi, R. Liu, K. Liang, L. Zhao, J. J. Gooding, C. Boyer and Z. Gu, *J. Colloid Interface Sci.*, 2018, **521**, 242.

25 M. Díaz-García, Á. Mayoral, I. Díaz and M. Sánchez-Sánchez, *Cryst. Growth Des.*, 2014, **14**, 2479.

26 V. K. Yachandra, V. J. Derose, M. J. Latimer, I. Mukerji, K. Sauer and M. P. Klein, *Science*, 1993, **260**, 675.

27 E. J. Martinze-Finley, S. Chakraborty and M. Aschner, in *Encyclopedia of Metalloproteins*, ed. R. H. Kretsinger, V. N. Uversky and E. A. Permyakov, Springer, New York, 2017, pp. 1227–1469.

28 S. Y. Yin, G. S. Song, Y. Yang, Y. Zhao, P. Wang, L. M. Zhu, X. Yin and X. B. Zhang, *Adv. Funct. Mater.*, 2019, **29**, 1901417.

29 Y. Y. Chen, H. Zhong, J. B. Wang, X. Y. Wan, Y. H. Li, W. Pan, N. Li and B. Tang, *Chem. Sci.*, 2019, **10**, 5773.

30 X. Qian, J. Zhang, Z. Gu and Y. Chen, *Biomaterials*, 2019, **211**, 1.

31 Y. Liu, M. Zhang and W. Bu, *View*, 2020, **1**, e18.